



Ripple Patterns in In-plane Velocities of OB Stars from LAMOST and *Gaia*

Xinlun Cheng¹, Chao Liu², Shude Mao^{1,3}, and Wenyuan Cui⁴¹ Physics Department and Tsinghua Centre for Astrophysics, Tsinghua University, Beijing 100084, People's Republic of China; liuchao@nao.cas.cn² Key Laboratory for Optical Astronomy, National Astronomical Observatories, Chinese Academy of Sciences, Beijing 100012, People's Republic of China³ National Astronomical Observatories, Chinese Academy of Sciences, 20A Datun Road, Chaoyang District, Beijing 100012, People's Republic of China⁴ Department of Physics, Hebei Normal University, Shijiazhuang 050024, People's Republic of China

Received 2018 December 6; revised 2019 January 21; accepted 2019 January 26; published 2019 February 6

Abstract

With about 12,000 OB type stars selected from the LAMOST and *Gaia* survey, we study their three-dimensional velocity distribution over the range of galactocentric radius from 6 to 15 kpc in the Galactic disk plane. A clear ripple pattern in the radial velocity (V_R) map is shown. The median V_R reaches -8 km s^{-1} at $R \sim 9 \text{ kpc}$, then increases to $\sim 0 \text{ km s}^{-1}$ at $R \sim 12 \text{ kpc}$, and later declines to below -10 km s^{-1} beyond $R \sim 13 \text{ kpc}$. The median azimuthal velocity (V_ϕ) map shows a similar pattern but has roughly one-quarter phase difference with the radial velocity. Although the ripple of negative V_R at $\sim 9 \text{ kpc}$ extends to about 40° in the azimuth angle, it does not align with either the Local or the Perseus spiral arms. Moreover, the farther ripple beyond 13 kpc does not match the Outer spiral arm either. This indicates that the non-axisymmetric kinematic features are not induced by perturbations of known spiral structures. The central rotating bar cannot lead to such patterns in the outer disk either. External perturbation of a dwarf galaxy or a dark matter sub-halo can induce such patterns, but this requires more evidence from both observations and simulations. The V_ϕ map in the Z - V_Z plane of the OB stars is also investigated. Despite asymmetry to some degree, no spiral pattern is found. This is reasonable as most of the OB stars have ages that are much younger than 100 Myr, which is smaller than one orbital period around the Galactic center.

Key words: Galaxy: disk – Galaxy: kinematics and dynamics – Galaxy: structure

1. Introduction

Following the *Gaia* second data release (DR2), the phase-mixing features in the Z - V_Z phase space of the Milky Way was discovered (Antoja et al. 2018) and confirmed (Bland-Hawthorn et al. 2019; Tian et al. 2018). This is likely caused by the perturbation of a satellite galaxy passing through the Galactic disk. Antoja et al. (2018) suggested that the encounter with the dwarf galaxy happened between 300 and 900 Myr ago, while Tian et al. (2018) and Bland-Hawthorn et al. (2019) favored the theory that the event occurred ~ 500 Myr ago.

The possible effect of interaction with satellite galaxies has already been explored (Edelsohn & Elmegreen 1997). Since the discovery of the phase-mixing phenomenon, both toy-models and N -body simulations have been performed, and it was found that the external perturber may induce coupled effects in both vertical and in-plane directions (D’Onghia et al. 2016; Binney & Schönrich 2018; Laporte et al. 2018a, 2018b; Bland-Hawthorn et al. 2019).

In addition, non-axisymmetric features in the velocity and density distributions have also been explored. The radial velocity, V_R , asymmetry was first detected with stars from the Radial Velocity Experiment (RAVE) survey (Siebert et al. 2011), and later confirmed with various stellar tracers from different surveys (Carlin et al. 2013; Williams et al. 2013; Sun et al. 2015a; Tian et al. 2017; Katz et al. 2018; Liu et al. 2018). Various theoretical explanations have been offered: perturbation by the central rotating bar (Fux 2001; Tian et al. 2017; Liu et al. 2018), spiral arms (Siebert et al. 2012; Katz et al. 2018), or a merging satellite galaxy (Carlin et al. 2013).

Vertical density and velocity oscillations have also been extensively studied (e.g., Widrow et al. 2012; Carlin et al. 2013; Sun et al. 2015a; Xu et al. 2015; Wang et al. 2018a, 2018b; Bennett & Bovy 2019). Theoretical explanations have

been proposed, including the interaction with the Sagittarius (Gómez et al. 2013) and vertical perturbation by spiral structures (Nelson 1976; Debattista 2014; Faure et al. 2014).

It is noted that most previous studies are based on old stellar populations with an age of at least 1 Gyr. Investigating asymmetric kinematics in young populations can play an important role because they can reflect the perturbed kinematics of the gaseous disk. In this Letter we use OB stars, which have ages from a few million to a few tens of millions years, to explore asymmetric motions in the three-dimensional velocity map beyond 6 kpc from the Sun in the Galactic plane.

This Letter is organized as follows. The procedure for data selection and analysis is in Section 2, results and discussions are in Section 3, and conclusions are drawn in Section 4.

2. Data

The data are combined with parameters from two surveys, line-of-sight velocities from LAMOST fifth data release (DR5; Deng et al. 2012; Zhao et al. 2012; Luo et al. 2015) and proper motions from the *Gaia* DR2 (Gaia Collaboration et al. 2016, 2018). We employed around 16,000 OB stars with spectral signal-to-noise ratio (S/N) larger than 15 selected from LAMOST DR5 (Liu et al. submitted). The distances of these OB stars are derived by Bailer-Jones et al. (2018). To keep the reliability of the distances, we only use OB stars with relative distance uncertainty $\sigma_d/d < 0.4$, in which d and σ_d are distance and its uncertainty. In fact, most stars have $0.07 < \sigma_d/d < 0.15$, which is considerably lower than the cutoff value (0.4).

Radial velocity was derived from $H\delta$ and $H\gamma$ absorption lines of the stellar spectra by using a forward model based on TLUSTY synthetic spectra library (Lanz & Hubeny 2007) conducted by Z. C. L. Liu et al. (2019, in preparation). Given effective temperature, surface gravity, metallicity, radial

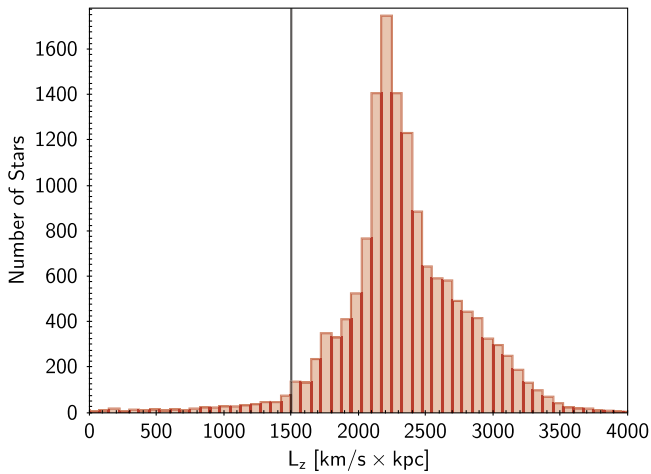


Figure 1. Distribution of L_z of OB star candidates before selection. We exclude possible contamination with $L_z < 1500 \text{ km s}^{-1} \text{ kpc}^{-1}$ indicated with the black line.

velocity, and stellar rotation, this model can predict $H\delta$ and $H\gamma$ line profiles. The radial velocity and other stellar parameters of the spectrum in interest can be determined by comparing to the predicted lines. The typical uncertainty of radial velocity is $\sim 5 \text{ km s}^{-1}$.

The three velocity components in Galactocentric cylindrical coordinates, V_R , V_ϕ , and V_Z , are calculated from the radial velocity, distance, and proper motions adopting that the motion of the Sun with respect to the local standard of rest (LSR) is $(9.58, 10.52, 7.01) \text{ km s}^{-1}$ (Tian et al. 2015) and the rotational speed of LSR at $V_{\text{LSR}} = 238 \text{ km s}^{-1}$ (Reid et al. 2014).

Most OB stars are massive stars in the disk and as young as a few tens of millions years, whereas a few low-mass post-AGB and blue horizontal branch stars from the halo population are contaminations. It is not easy to distinguish them from low-resolution spectra, but they can be identified by locations and kinematics. We only select stars within $|Z| < 1.0 \text{ kpc}$ and with large enough angular momenta with respect to the Z-axis (L_z). Figure 1 shows the distribution of L_z . Only a small fraction of stars have low L_z , which may be from the thick disk or the halo. We thus empirically exclude stars with $L_z < 1500 \text{ km s}^{-1} \text{ kpc}^{-1}$.

We arbitrarily select one spectrum for stars with multiple observations, and obtain 12,360 OB stars after the above selections. Their spatial distribution in the X - Y plane is illustrated in Figure 2. The galactocentric coordinates are selected such that the Sun is at $X = 8.34 \text{ kpc}$ and $Y = 0 \text{ kpc}$. The locations of spiral arms are from Reid et al. (2014) and Sun et al. (2015b). The number density is obtained using the adaptive probability density estimation method with a bi-weight kernel (Skuljan et al. 1999). For our sample, the optimal value for the smoothing parameter is $h = 0.788 \text{ kpc}$.

3. Results

3.1. Ripple Patterns in the Velocity Map

Figures 3(a), (c), and (e) show the velocity fields of \tilde{V}_R , \tilde{V}_ϕ , and \tilde{V}_Z , respectively, estimated with the same technique as for the number density, while panels (b), (d), and (f) show the uncertainties of the corresponding velocity fields estimated from bootstrapping. We arbitrarily selected 80% of the stars as a subsample and added corresponding Gaussian noise to their velocities. The adaptive probability density estimation was

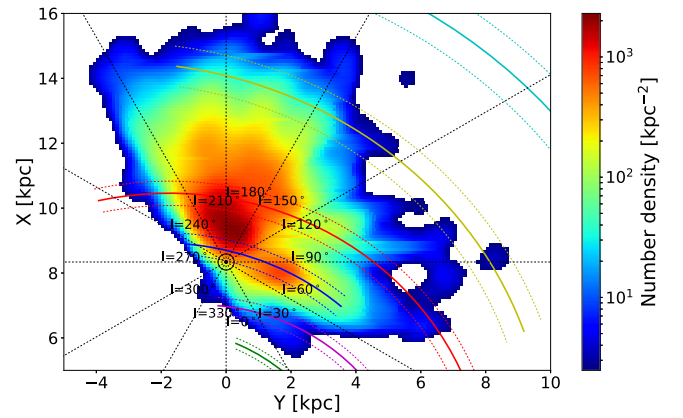


Figure 2. Spatial distribution of the OB stars in the Galactic plane. The Sun marked as \odot is located at $(X = 8.34, Y = 0) \text{ kpc}$. Spiral structures, i.e., Scutum, Sagittarius, Local, Perseus, Outer, and a new spiral arm, are indicated from the Galactic Center (GC) outwards as solid colored curves. The dotted curves around the solid ones are the uncertainties of the corresponding spiral arms. Their locations are adopted from Reid et al. (2014) and Sun et al. (2015b). The black dotted lines represent different Galactic longitudes.

rebuilt for this subsample to derive the velocity fields. The process was repeated 1000 times, and the standard deviations at each point in the X - Y plane are calculated and taken as uncertainties. Note that they are different from the velocity dispersions by definition.

We integrated the three velocity fields within $-2.5 < Y < 2.5 \text{ kpc}$ and plotted the average velocity with respect to X in Figure 4 to better illustrate the radial variation of velocities. The uncertainties are estimated with the same methods as mentioned above.

3.1.1. Asymmetry in V_R

A few local ripple-like patterns are identified in the map of \tilde{V}_R Figure 3(a). That is, \tilde{V}_R displays with two negative-velocity strips (blue) with a zero-value strip in between. At $X \sim 9 \text{ kpc}$, \tilde{V}_R declines to $\sim -8 \text{ km s}^{-1}$, and increases back to ~ 0 at around $X = 12 \text{ kpc}$, and finally drops to below -10 km s^{-1} when $X > 15 \text{ kpc}$. Both negative \tilde{V}_R features are detected with a $> 5\sigma$ confidence level according to the map of $\epsilon_{\tilde{V}_R}$ shown in Figure 3(b). These features are better shown in Figure 4 with the red lines.

Compared to the spiral arms, the ripple patterns are not aligned with them in the X - Y plane. The near negative \tilde{V}_R strip overlaps with the Local Arm at $(X \sim 9, Y \sim 0) \text{ kpc}$. It does not follow the arm to $(X = 7.5, Y = 3.5) \text{ kpc}$, but extends along $X \sim 9 \text{ kpc}$ and overlaps with part of the Perseus Arm at $Y \sim 3 \text{ kpc}$. At $Y > 3 \text{ kpc}$, it goes beyond the Perseus Arm. Similarly, the farther negative \tilde{V}_R strip is located at larger radius than the Outer Arm. In the bottom row of Figure 3, we tested the robustness of the ripple as a function of distance uncertainty. We cut the data with $\sigma_d/d < 0.1, 0.2$, and 0.5 . The 9 kpc \tilde{V}_R strip exists in all three cases and shows similar trend for the case with $\sigma_d/d < 0.2$. This strongly indicates that the pattern is real.

The strip centered at $X = 9 \text{ kpc}$ is consistent with previous discoveries (Siebert et al. 2011; Carlin et al. 2013; Liu et al. 2017b, 2018; Tian et al. 2017; Katz et al. 2018). Siebert et al. (2012) and Katz et al. (2018) suggested that this asymmetric radial velocity is produced by the perturbation of nearby spiral structures. Theoretical studies (Debattista 2014; Faure et al. 2014)

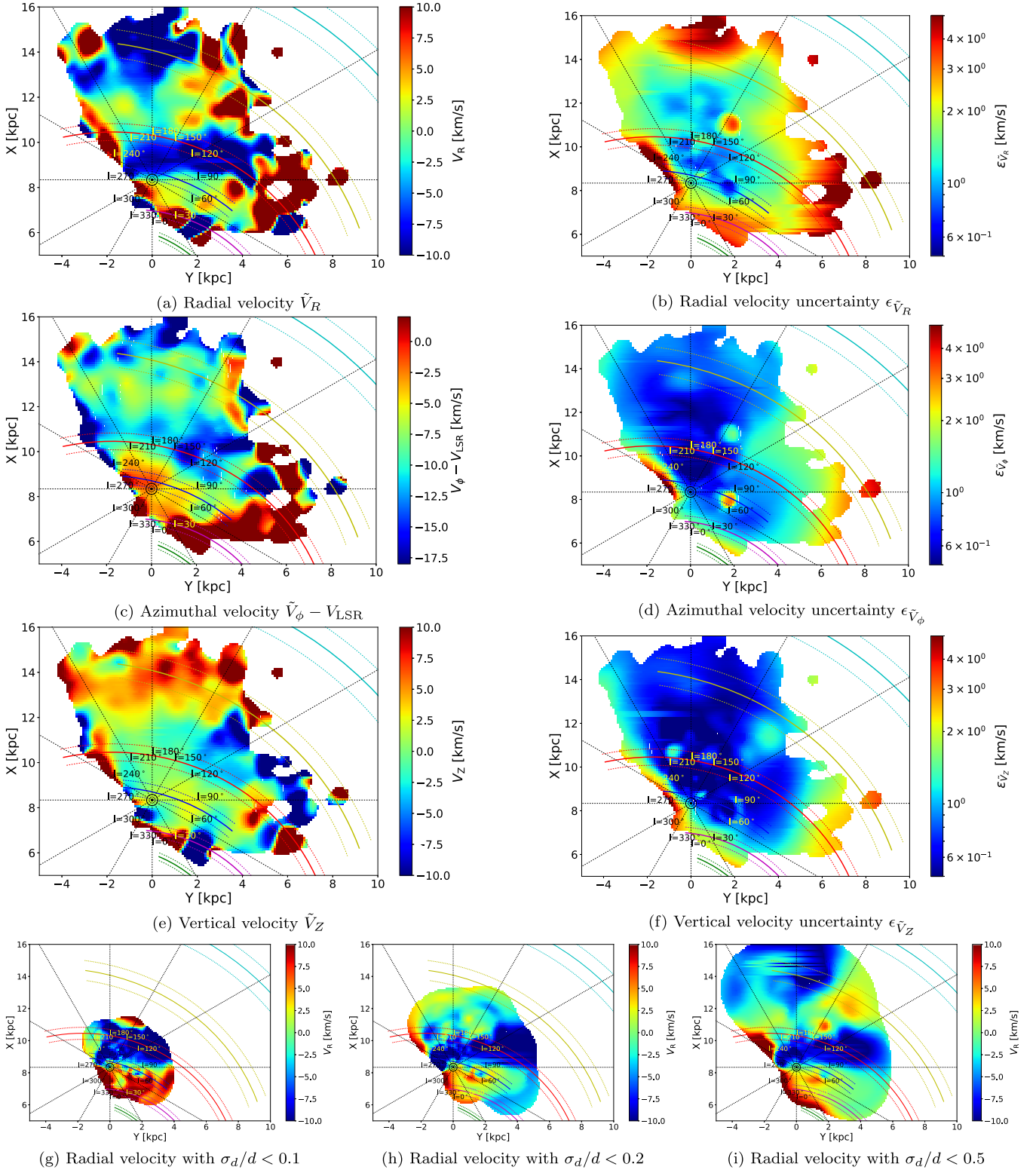


Figure 3. Figure (a), (c), and (e) are the maps of velocity components, \tilde{V}_R , \tilde{V}_ϕ , and \tilde{V}_Z from top to bottom, respectively, Figures (b), (d), and (f) are their respective uncertainties. The bottom row tests the \tilde{V}_R maps of the stars with $\sigma_d/d < 0.1, 0.2$ and 0.5 in (g), (h), and (i), respectively. The Sun is located at $(X = 8.34, Y = 0)$ kpc and is marked as \odot . The solid curves indicate the spiral structures as in Figure 2. The dotted lines represent different Galactic longitudes.

found that if this is the case, then the spatial distribution of the asymmetric \tilde{V}_R should be naturally correlated with the coherent spiral structures. Therefore, the uncorrelated spatial distribution between the negative \tilde{V}_R strip and the Local Arm or Perseus Arm

shows that the perturbation of the spiral arms is not the main driver of the ripples.

Compared to D’Onghia et al. (2016), we find that the ripple patterns are similar to their simulations (see the top-right plot in

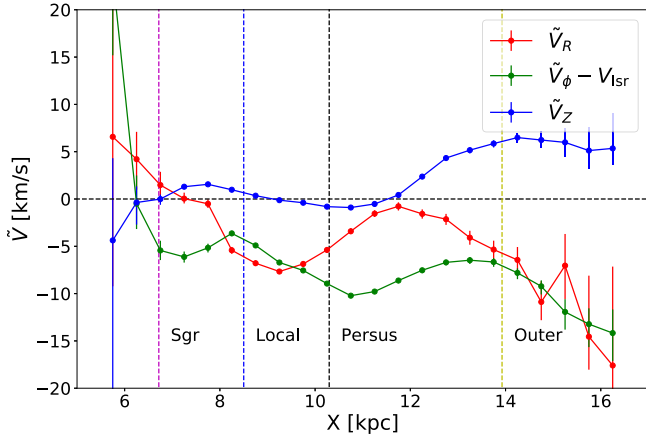


Figure 4. Average velocities with respect to X with stars in $-2.5 < Y < 2.5$ kpc. The average positions of spiral arms are indicated with dotted vertical lines.

their Figure 4), which demonstrate a perturbed disk by an interaction with a satellite.

Note that the strip at $X > 15$ kpc approaches the regime that the parallax from *Gaia* is less precise. The larger uncertainties of parallax and the uncertainties of proper motions have been considered in the estimation of the uncertainty of \tilde{V}_R shown in Figure 3(b). According to this figure, the typical error of the median radial velocity at $X \sim 15$ kpc is around $3\text{--}4 \text{ km s}^{-1}$. The smaller values of error are mostly due to two reasons. First, the radial velocity is mostly contributed by the line-of-sight velocity derived from the LAMOST spectra, which is independent of parallax. Second, the large number of OB stars detected reduces the uncertainty of the velocity, even though the typical error of the line-of-sight velocity is $\sim 5 \text{ km s}^{-1}$. Therefore, the strip shown at $X > 15$ kpc is real. Similar to the strip displayed at $X \sim 9$ kpc, the misalignment of the farther strip with the Outer Arm implies that the spiral arms are not responsible for the ripples.

3.1.2. Asymmetry in $\tilde{V}_\phi - V_{\text{LSR}}$ and \tilde{V}_Z

Similar ripple patterns are also seen in $\tilde{V}_\phi - V_{\text{LSR}}$, as shown in Figures 3(c) and 4 (green line). Unlike \tilde{V}_R , $\tilde{V}_\phi - V_{\text{LSR}}$ shows three dips at around $X = 7$, 11 kpc, and >15 kpc. We can conclude from Figure 4 that the ripple of $\tilde{V}_\phi - V_{\text{LSR}}$ has roughly one-quarter phase difference with the ripple of \tilde{V}_R . It clearly shows that the dip of $\tilde{V}_\phi - V_{\text{LSR}}$ at $X \sim 11$ kpc is located between the dip of \tilde{V}_R at ~ 9 kpc and the peak of \tilde{V}_R at ~ 12 kpc. Meanwhile, the local peak of $\tilde{V}_\phi - V_{\text{LSR}}$ at around 13 kpc is beyond the peak of \tilde{V}_R located at ~ 12 kpc.

Indeed, if the disturber, internal (e.g., spiral structure) or external (e.g., a dwarf galaxy), introduces an in-plane gravitational force to the stars, the decomposition of the perturbation force along the radial and azimuthal direction would naturally induce additional radial and azimuthal motions with one-quarter phase difference to the stars.

Liu et al. (2017b) showed a similar azimuthal velocity map with young stars. However, because their map of young F-type stars only covers less than 1 kpc around the Sun, they did not find that the velocity pattern is unrelated to the Local Arm at larger distance.

The ripple pattern is not clearly displayed in the distribution of the vertical velocity, but other interesting features are seen

in the \tilde{V}_Z map. A region with a relatively high upward motion ($>5 \text{ km s}^{-1}$) beyond $X = 13$ kpc is discovered with $3 \sim 5\sigma$ confidence level (see Figure 3(e) and more clearly in Figure 4).

Liu et al. (2017a) discovered a similar vertical motion using red clump stars along the Galactic anti-center direction and attributed it to the Galactic warp. Poggio et al. (2018) reported a gradient of similar scale at 8–14 kpc. Furthermore, similar to their findings, the upward vertical velocity also shows a larger amplitude in the second quadrant of the disk plane, i.e., $Y > 0$ in our coordinates. This implies that the line-of-node of the warp may be located in the third quadrant.

3.1.3. A Substructure along $l = 90^\circ$?

In addition to the features discussed above, a suspected substructure is found in the velocity map along the Galactic longitude of $l = 90^\circ$ beyond $Y > 5$ kpc along the longitude. The OB stars in this region show $\tilde{V}_R > +10 \text{ km s}^{-1}$, $\tilde{V}_\phi - V_{\text{LSR}} < -15 \text{ km s}^{-1}$, and $\tilde{V}_Z < -5 \text{ km s}^{-1}$. In other words, this group of stars is moving away from the Galactic center and downward to the south with slower azimuthal velocity. The feature is close to the edge of the detection of the sample. Therefore, it is not clear whether or not this is real.

3.2. Spiral Feature in the Phase Space

Following Tian et al. (2018), who tried to find the spiral feature in the phase space for younger stars so that the time of the occurrence of the perturbation can be better constrained, we examine the distribution of \tilde{V}_ϕ in the Z - V_Z phase space with our samples.

Figure 5(a) shows the map of the median \tilde{V}_ϕ with subtraction of V_{LSR} in the Z - V_Z plane for all OB stars, while Figure 5(b) displays the similar map but only with stars in the same cylinder selected by Bland-Hawthorn et al. (2019). We see that $\tilde{V}_\phi - V_{\text{LSR}}$ varies in the Z - V_Z plane with amplitude of $4 \sim 8 \text{ km s}^{-1}$. The lowest $\tilde{V}_\phi - V_{\text{LSR}}$ ($-2 \sim -4 \text{ km s}^{-1}$) appears at ($Z \sim -0.25$ kpc, $\tilde{V}_Z \sim 0 \text{ km s}^{-1}$), and the highest values ($2 \sim 4 \text{ km s}^{-1}$) appear at roughly the mirroring position of the lowest region with respect to $Z = 0$. However, it does not show a clear spiral pattern as is seen in other works. This is reasonable because the OB stars are too young to finish even one orbital period around the Galactic center.

4. Discussions and Conclusions

It seems that the ripple patterns in the map of in-plane velocities is the result of a perturbation. In principle, the disturber could be classified as internal, such as spiral structures, giant molecular clouds, or a central rotating bar, or external, such as pass-by dwarf galaxies or dark matter sub-halos. In this section we attempt to briefly discuss these possibilities in turn.

As discussed in the previous section, it is clear that the ripple patterns shown in the map of \tilde{V}_R and \tilde{V}_ϕ do not follow the present-day gaseous spiral arms. Thus, they are the result of perturbations induced by current spiral structures according to Siebert et al. (2012). However, it is noted that they assume a steady spiral structure in their simulation, while the origin of the spiral structures is far from clear (Baba et al. 2018; Sellwood et al. 2019; Tchernyshyov et al. 2018). Therefore, our results may not clearly exclude the perturbation of spiral arms that originated from other mechanism, but only rule out a steady-density wave spiral structure.

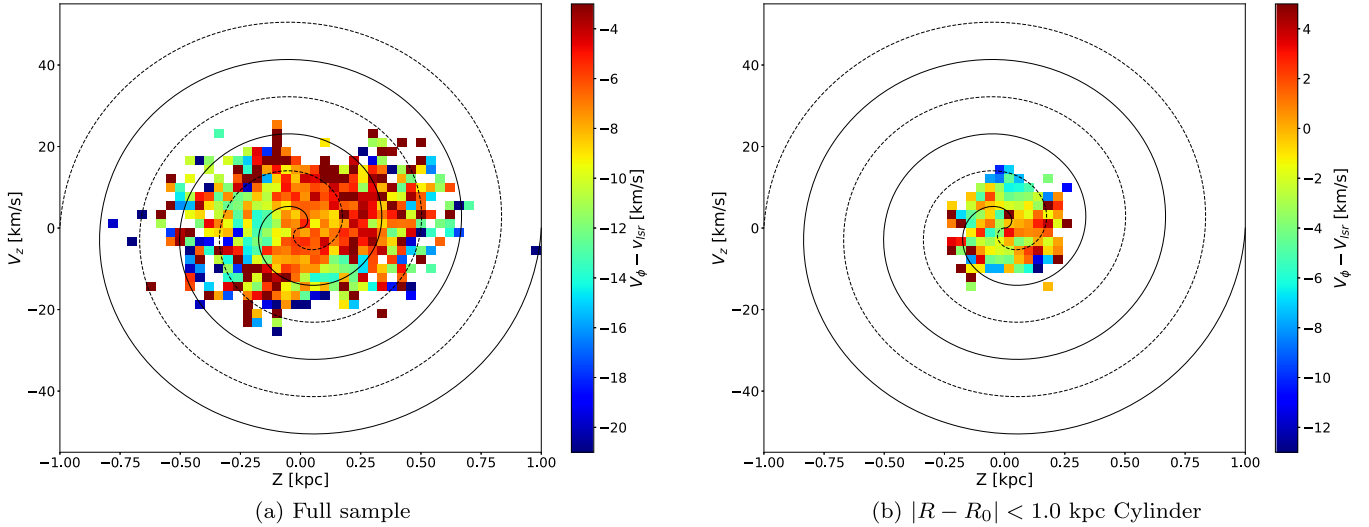


Figure 5. $\tilde{V}_\phi - V_{\text{LSR}}$ in the Z - V_Z phase space. The solid and dashed lines indicate the spiral reported by Bland-Hawthorn et al. (2019), with the solid line as the high peak and the dashed line as the valley between peaks. The left panel is for the full sample, while the right panel is for stars within 1 kpc of the Sun.

Liu et al. (2018) revealed that a bar with pattern speed of $60 \text{ km s}^{-1} \text{ kpc}^{-1}$ is also capable of producing the dip in \tilde{V}_R centered at $X \sim 9 \text{ kpc}$ through a test particle simulation, but could not produce the farther decline beyond 13 kpc. Thus, the bar alone is not the reason.

Giant molecular clouds may also be potential disturbers and can induce spiral structures, according to D’Onghia et al. (2013). However, this scenario cannot be investigated until more simulations examining how giant molecular clouds affect the stellar kinematics are performed.

Considering the external disturbers, many recent works in Section 1 argued that Sagittarius is one of the possible disturbers. However, it is unlikely that these OB stars were directly affected due to their young age. Instead, the encounter might affect the gaseous disk, which may eventually affect the orbits of the OB stars that have formed from it. As pointed out by Binney & Schönrich (2018) and Bland-Hawthorn et al. (2019), the pass-by satellite attracts the disk stars both in vertical and in-plane direction. The in-plane perturbation may raise complicated spiral structures with rich ripple-like in-plane velocities as seen in the simulation by Bland-Hawthorn et al. (2019; see their Figure 25). Unlike the stellar disk, dissipation may play an important role in the gaseous disk.

As a qualitative estimate, the speed of sound can be used to obtain an approximate time timescale of dissipation. The cold neutral medium (CNM) has a typical temperature of $T = 100 \text{ K}$ and hydrogen inside is in atomic state (Ferrière 2001). Thus, we can treat CNM as ideal gas and estimate the speed of sound in adiabatic and isothermal processes.

$$V_{\text{ad}} = \sqrt{\frac{\gamma kT}{m}} = 1.2 \text{ km s}^{-1}, \quad (1)$$

$$V_{\text{iso}} = \sqrt{\frac{kT}{m}} = 0.9 \text{ km s}^{-1}, \quad (2)$$

where $\gamma = 5/3$ for hydrogen in atomic state, k is the Boltzmann constant, and m is the mass of the hydrogen atom. Thus, $V_{\text{sound}} = 1 \text{ km s}^{-1}$ is a reasonable approximation for the speed of sound in the CNM.

The scale height of HI region at the position of the Sun is $\sim 0.15 \text{ kpc}$ (Kalberla & Kerp 2009). Therefore, a vertical

perturbation would dissipate in a timescale of

$$\tau_{\text{vertical}} = \frac{H_{\text{vertical}}}{V_{\text{sound}}} = \frac{150 \text{ pc}}{1 \text{ km s}^{-1}} \approx 150 \text{ Myr}. \quad (3)$$

Considering that the encounter was $\sim 500 \text{ Myr}$ ago, it is possible that a great proportion of the vertical impact in the gaseous disk has been dissipated. This can explain the lack of spiral features in the vertical phase space shown in Figure 5(a).

On the other hand, the in-plane perturbation due to the encountering satellite can induce spiral structures in the gaseous disk, similar to the stellar disk. However, due to dissipation of the gas, the spiral structures may be finally damped as mentioned in Section 6.4 of Binney & Tremaine (2008). A very rough estimate of the timescale of dissipation in the in-plane direction can be made using the size of the gaseous disk and the speed of sound. Considering the scale length of gaseous disk is $\sim 3.15 \text{ kpc}$ (Kalberla & Kerp 2009), the timescale of dissipation can be approximated as

$$\tau_{\text{H}} = \frac{H_r}{V_{\text{sound}}} = \frac{3.15 \text{ kpc}}{1 \text{ km s}^{-1}} \approx 3.1 \text{ Gyr}. \quad (4)$$





This means that although a perturbation to the disk occurred a few hundred Myr ago, the marks of the in-plane perturbation sculpted in the gaseous disk may later be inherited by the newborn OB stars from these gas clouds.

An alternative scenario is that another dark matter sub-halo disturbed the disk a few tens of Myr ago and imprinted the ripple pattern in these young stars. If this is the case, similar patterns should also be seen in relatively old stellar populations.

In summary, we explored the kinematic structure of the Milky Way galaxy with OB stars. While they do not show a clear indication of the phase-mixing spiral in the Z - V_Z plane, we found clear ripple patterns in the in-plane map of \tilde{V}_R and \tilde{V}_ϕ . The roughly one-quarter phase difference between the ripple features in \tilde{V}_R and \tilde{V}_ϕ implies that these patterns should be a result of an in-plane perturbation. We considered a few possible disturbers, including internal and external origins, and find that neither of them can be the exclusive reason for the ripple structure, although perturbation of stationary spiral structures can be ruled out as the ripples are not aligned with the known spiral structures.

We appreciate the anonymous referee for his/her helpful suggestions that improved this Letter. We thank Youjun Lu, Zhao-Yu Li, Juntao Shen, and Elena D’Onghia for helpful discussions and comments. This work is supported by the National Key Basic Research and Development Program of China No. 2018YFA0404501 and NFSC under grants 11821303, 11390372, 11761131004 (S.M.), 11333003 (C.L. and S.M.), 11873057 (C.L.), and 11773009 (W.C.). Guoshoujing Telescope (the Large Sky Area Multi-Object Fiber Spectroscopic Telescope LAMOST) is a National Major Scientific Project built by the Chinese Academy of Sciences. Funding for the project has been provided by the National Development and Reform Commission. LAMOST is operated and managed by the National Astronomical Observatories, Chinese Academy of Sciences. This work has made use of data from the European Space Agency (ESA) mission *Gaia* (<https://www.cosmos.esa.int/gaia>), processed by the *Gaia* Data Processing and Analysis Consortium (DPAC, <https://www.cosmos.esa.int/web/gaia/dpac/consortium>). Funding for the DPAC has been provided by national institutions, in particular the institutions participating in the *Gaia* Multilateral Agreement.

ORCID iDs

Xinlun Cheng  <https://orcid.org/0000-0002-7009-3957>
 Chao Liu  <https://orcid.org/0000-0002-1802-6917>
 Shude Mao  <https://orcid.org/0000-0001-8317-2788>
 Wenyan Cui  <https://orcid.org/0000-0003-1359-9908>

References

- Antoja, T., Helmi, A., Romero-Gomez, M., et al. 2018, *Natur*, **561**, 360
 Baba, J., Kawata, D., Matsunaga, N., Grand, R. J. J., & Hunt, J. A. S. 2018, *ApJL*, **853**, L23
 Bailer-Jones, C. A. L., Rybizki, J., Foesneau, M., Mantelet, G., & Andrae, R. 2018, *AJ*, **156**, 58
 Bennett, M., & Bovy, J. 2019, *MNRAS*, **482**, 1417
 Binney, J., & Schönrich, R. 2018, *MNRAS*, **481**, 1501
 Binney, J., & Tremaine, S. 2008, *Galactic Dynamics: Second Edition* (Princeton, NJ: Princeton Univ. Press)
 Bland-Hawthorn, J., Sharma, S., Tepper-Garcia, T., et al. 2019, *MNRAS*, in press (arXiv:1809.02658)
 Carlin, J. L., DeLaunay, J., Newberg, H. J., et al. 2013, *ApJL*, **777**, L5
 Debattista, V. P. 2014, *MNRAS*, **443**, L1
 Deng, L.-C., Newberg, H. J., Liu, C., et al. 2012, *RAA*, **12**, 735
 D’Onghia, E., Madau, P., Vera-Ciro, C., Quillen, A., & Hernquist, L. 2016, *ApJ*, **823**, 4
 D’Onghia, E., Vogelsberger, M., & Hernquist, L. 2013, *ApJ*, **766**, 34
 Edelsohn, D. J., & Elmegreen, B. G. 1997, *MNRAS*, **287**, 947
 Faure, C., Siebert, A., & Famaey, B. 2014, *MNRAS*, **440**, 2564
 Ferrière, K. M. 2001, *RvMP*, **73**, 1031
 Fux, R. 2001, *A&A*, **373**, 511
 Gaia Collaboration, Brown, A. G. A., Vallenari, A., et al. 2018, *A&A*, **616**, A1
 Gaia Collaboration, Prusti, T., de Bruijne, J. H. J., et al. 2016, *A&A*, **595**, A1
 Gómez, F. A., Minchev, I., O’Shea, B. W., et al. 2013, *MNRAS*, **429**, 159
 Kalberla, P. M. W., & Kerp, J. 2009, *ARA&A*, **47**, 27
 Katz, D., Antoja, T., Romero-Gómez, M., et al. 2018, *A&A*, **616**, A11
 Lanz, T., & Hubeny, I. 2007, *ApJS*, **169**, 83
 Laporte, C. F. P., Johnston, K. V., Gómez, F. A., Garavito-Camargo, N., & Besla, G. 2018b, *MNRAS*, **481**, 286
 Laporte, C. F. P., Minchev, I., Johnston, K. V., & Gómez, F. A. 2018a, arXiv:1808.00451
 Liu, C., Tian, H.-J., & Wan, J.-C. 2017a, in IAU Symp. 321, Formation and Evolution of Galaxy Outskirts, ed. A. Gil de Paz, J. H. Knapen, & J. C. Lee (Cambridge: Cambridge Univ. Press), 6
 Liu, C., Xu, Y., Wang, H., & Wan, J. 2018, in IAU Symp. 334, Rediscovering Our Galaxy, ed. C. Chiappini et al. (Cambridge: Cambridge Univ. Press), 109
 Liu, C., Wang, Y.-G., Shen, J., et al. 2017b, *ApJL*, **835**, L18
 Luo, A. L., Zhao, Y.-H., Zhao, G., et al. 2015, *RAA*, **15**, 1095
 Nelson, A. H. 1976, *MNRAS*, **177**, 265
 Poggio, E., Drimmel, R., Lattanzi, M. G., et al. 2018, *MNRAS*, **481**, L21
 Reid, M. J., Menten, K. M., Brunthaler, A., et al. 2014, *ApJ*, **783**, 130
 Sellwood, J. A., Trick, W., Carlberg, R., Coronado, J., & Rix, H.-W. 2019, *MNRAS*, in press (arXiv:1810.03325)
 Siebert, A., Famaey, B., Binney, J., et al. 2012, *MNRAS*, **425**, 2335
 Siebert, A., Famaey, B., Minchev, I., et al. 2011, *MNRAS*, **412**, 2026
 Skuljan, J., Hearnshaw, J. B., & Cottrell, P. L. 1999, *MNRAS*, **308**, 731
 Sun, N.-C., Liu, X.-W., Huang, Y., et al. 2015a, *RAA*, **15**, 1342
 Sun, Y., Xu, Y., Yang, J., et al. 2015b, *ApJL*, **798**, L27
 Tchernyshyov, K., Peek, J. E. G., & Zasowski, G. 2018, *AJ*, **156**, 248
 Tian, H.-J., Liu, C., Carlin, J. L., et al. 2015, *ApJ*, **809**, 145
 Tian, H.-J., Liu, C., Wan, J.-C., et al. 2017, *RAA*, **17**, 114
 Tian, H.-J., Liu, C., Wu, Y., Xiang, M.-S., & Zhang, Y. 2018, *ApJL*, **865**, L19
 Wang, H., López-Corredoira, M., Carlin, J. L., & Deng, L. 2018a, *MNRAS*, **477**, 2858
 Wang, H.-F., Liu, C., Xu, Y., Wan, J.-C., & Deng, L. 2018b, *MNRAS*, **478**, 3367
 Widrow, L. M., Gardner, S., Yanny, B., Dodelson, S., & Chen, H.-Y. 2012, *ApJL*, **750**, L41
 Williams, M. E. K., Steinmetz, M., Binney, J., et al. 2013, *MNRAS*, **436**, 101
 Xu, Y., Newberg, H. J., Carlin, J. L., et al. 2015, *ApJ*, **801**, 105
 Zhao, G., Zhao, Y.-H., Chu, Y.-Q., Jing, Y.-P., & Deng, L.-C. 2012, *RAA*, **12**, 723